College of Polymer Science and Polymer Engineering

9-2005

Branching in Electrospinning of Nanofibers

A. L. Yarin

W. Kataphinan

Darrell Hyson Reneker
University of Akron Main Campus, reneker@uakron.edu

Branching in electrospinning of nanofibers

A. L. Yarin

Faculty of Mechanical Engineering, Technion-Israel Institute of Technology, Haifa 32000, Israel

W. Kataphinan and D. H. Reneker[a)]

Maurice Morton Institute of Polymer Science, The University of Akron, 170 University Circle, Akron, Ohio 44325-3909

Electrospinning of polymer nanofibers often begins with a single, straight, elongating, and electrified fluid jet that emanates from a droplet tip when the electric field at the surface is high enough. After some distance an electrically driven bending instability of the elongating jet occurs. For a polymer solution suitable for electrospinning, capillary instability does not cause the jet to become a spray of droplets. Under some conditions, a sequence of secondary jet branches emanates from the primary jet. This paper describes an experiment in which many closely spaced branches along the jet were observed during the electrospinning of a polycaprolactone solution. A theoretical description of the branching phenomenon is proposed. © *2005 American Institute of Physics.* [DOI: 10.1063/1.2060928]

I. INTRODUCTION

Electrospinning[1,2] provides a straightforward electrohydrodynamical method to produce fibers with diameters in the range of 100 nm or less. Polymer solutions, liquid crystals, and suspensions of solid particles in polymer solutions were electrospun in an electric field of the order of 100 V/mm. The electric force causes an electrically charged jet of polymer solution to emanate from a supported drop. The path of the elongating and thinning jet is straight for a distance of several millimeters from the drop, and then the elongating jet begins to bend.[3,4] The electrical forces bend, stretch, and thin the jet by very large amounts causing the path of the jet to become complex. The solvent evaporates and the resulting dry polymer nanofibers can be collected as nonwoven mats[3] or as ordered arrays and ropes.[5,6] Nanofibers of both electrically insulating and electrically conducting polymers have been electrospun.[1–9]

Experimental and theoretical results[3,4] showed that electrospinning of polymer nanofibers typically involves a single, electrified, continuous, elongating, and bending jet. Branching of the jet into several smaller jets was also observed under some conditions for a number of polymer solutions including, for example, polyethylene oxide,[3] and polycaprolactone (PCL), the subject of this paper. Bending and branching may occur together or individually in a particular segment. It was demonstrated that particular kinds of polymer and solvent affect the occurrence of branching under the usual conditions of electrospinning. Formation of nanofibers with noncircular cross sections, including development of ribbonlike[10] fibers, was also observed during the electrospinning of solutions that exhibited a propensity for branching.

In the present work, the initial straight part and the bending part of electrospinning jets of polycaprolactone dissolved in acetone developed many lateral branches during electrospinning. A mechanism leading to the formation of nanofibers with noncircular cross sections and "undulating" surfaces is modeled. In Sec. II the experimental observations of secondary and tertiary jet branches during electrospinning of PCL are presented. Sections III and IV contain the theoretical description of the static, undulating, and equilibrium jet shapes. Section V deals with the growth, in time, of undulations on the surface in the framework of the linear stability theory. The theoretical results are discussed and compared to the experimental data in Sec. VI. Conclusions are drawn in Sec. VII.

II. EXPERIMENT

The apparatus and the polycaprolactone solutions prepared for this study were similar to those used in a previous work.[11] Polycaprolactone (PCL), chemical formula $[O(CH_2)_5CO]_n$, with a molecular weight of 120 000 g/mol was dissolved in acetone at concentrations near 15%. The observations are not sensitive to small variations in concentration. The polymer was purchased from Scientific Polymer Products, Inc. The experiments were done under ambient condition at room temperature and comfortable humidity (about 25% relative humidity).

Polymer solutions were electrospun from a drop hanging from a glass pipette with a tip opening in the range from 300 to 400 μm. Dried polymer at the tip sometimes formed a short, tubelike extension of the pipette, which affected the size and shape of the droplet, but branches were still observed. Branching jets, of 15 wt % PCL solutions, were produced when the electrical potential difference between the tip and the collector was in the range from 3 to 15 kV and the distance between the spinneret and ground was in the range from 15 to 70 mm (cf. Fig. 1). No stable jets were produced at 2 kV even after a jet was started by touching the drop with an insulating rod and pulling out a charged fluid segment. The electric-field strengths for the experiments described in this paper ranged from 57 to 500 V/mm. The volumetric

---

[a)]Electronic mail: reneker@uakron.edu
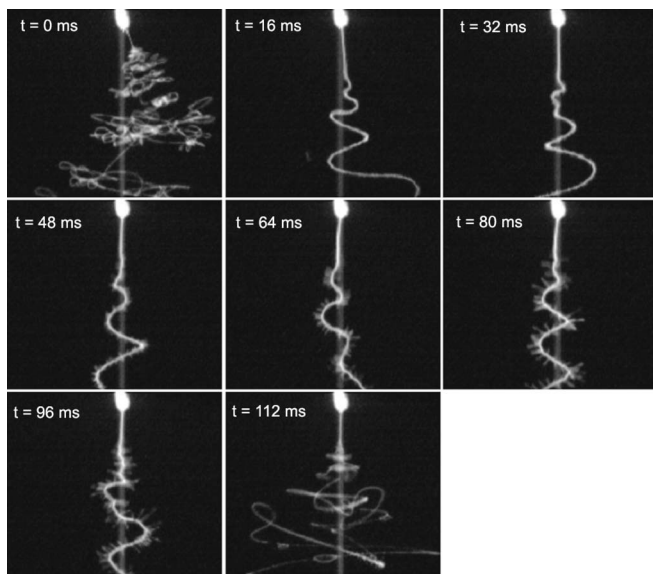
FIG. 1. Lateral jets from a PCL solution. These "stopped motion" images of a jet were taken by a high-speed camera at a frame rate of 2000 frames/s. Every 32nd frame is shown here, so the time separation between the frames shown was about 12 ms. The 15% PCL solution was electrospun at 5 kV, and the gap distance from pipette to copper plate collector was 70 mm. The width of each frame is about 14 mm. The exposure time of each frame was 0.1 ms. The positive z axis in the theoretical model points downward in these images. Branches are usually initiated in the straight segment and continue to elongate while the primary jet undergoes the electrically driven bending instability. The vertical gray line is due to light from the drop scattered by the camera. This line is not part of the jet. Stereographic images show that every segment of the primary jet including those segments where a branch is present moved radially outward and downward as the segment is elongated.

flow rate of the polymer solution varied slowly and cyclically but the variation was small during the short times required to observe a particular set of branches.

Jets issuing from the droplets of PCL solution at the open end of the pipette were photographed at rates up to 2000 frames/s with exposure times as short as 0.1 ms using a Motionscope from Redlake Imaging. The jets were illuminated with a xenon arc lamp in combination with a diffuser and a Fresnel lens.[3] Prisms were sometimes used[3] to produce stereographic images of the sort shown in Fig. 2(a). The lengths and position of the branches in three-dimensional space were measured and used to create stereographic diagrams as shown in Fig. 2(b). The vector direction of the branches is in the general direction of the local electric field at points near the surface of the jet, and the stereographic images show that the radial component of the field is larger than the axial component as assumed in the model.

All the measurements of the distance between branches in this paper were determined from two-dimensional images, since the collection of the stereographic information is laborious and produces only moderate improvement in the accuracy of the measurements. While the theory that follows predicts the distance between the places where branches were initiated, the measured distances include the amounts by which the segments between branches elongated before the jet solidified. For several typical jets, the distance between two adjacent branches was measured as a function of time starting at the frame in which the two branches were first
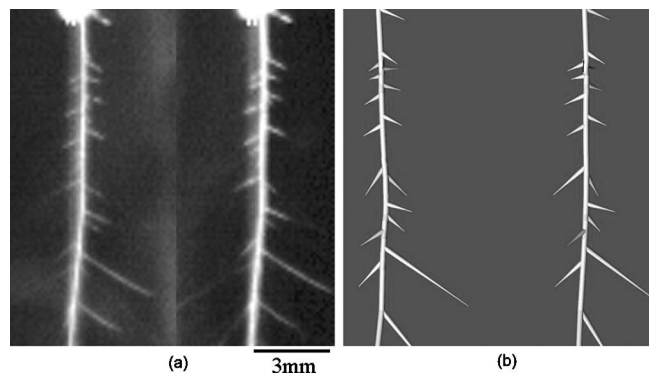
FIG. 2. (a) A stopped motion stereo image of branches on the straight segment taken by a high-speed optical camera at a frame rate of 2000 frames/s. The 15% PCL solution was electrospun at 5 kV. The gap distance from pipette to copper plate collector was 50 mm. The exposure time of each frame was 0.1 ms. The z axis points downward. (b) The stereographic image was reconstructed from the measurements of the x and y coordinates of the pairs of points, which could be identified in both the stereo images of the jet in (a), by using PHOTOMODELER and RHINO3D software programs (Ref. 33).

observed and continuing until one of the branches passed out of the field of view. The increase in the distance between adjacent branches was rapid at first and became much slower after the distance had doubled.

The observed azimuthal directions of the jet branches vary. An imperfect spiral is suggested by Fig. 2(b). Adjacent branches can lower their electrostatic interaction energy by extending in different azimuthal directions. Interactions between the branches and the charges on nearby loops of the primary jet may also affect the direction of a branch. The jet and the branches are tapered. Bending and branching may occur together. The stereographic image of the azimuthal directions of the branches provided reliable information about the location and direction of the branches in three-dimensional space.

The branches did not occur continuously. As time progressed, the field shown in Fig. 1 showed the following sequence of three types of events: (1) a straight segment, (2) the onset of the bending instability which usually generated a garland,[11] and (3) a nearly straight and relatively long segment on which the branches appeared. Branches grew rapidly after they appeared. This sequence of three events repeated about 10 times/s. The reasons for this repeating sequence are not presently known. Many such branching events were photographed. Branches were seen when the dried nanofibers were observed microscopically, but the tangled paths of the collected nanofibers made it impractical to measure the relatively long distance between the branches. For a particular branching event, a frame that showed a number of branches was selected. The spacings between adjacent branches were determined. Two significant figures were kept, which is consistent with the precision of the measurement. This measurement was repeated for each of the five to ten events that occurred within about 1 s. At each electrical field, the observed spacing between adjacent branches was calculated for each sequential pair of branches. These numbers were sorted into "bins" and used to create the histograms shown in Fig. 3. Each bin was 0.001 mm wide. If the branch-
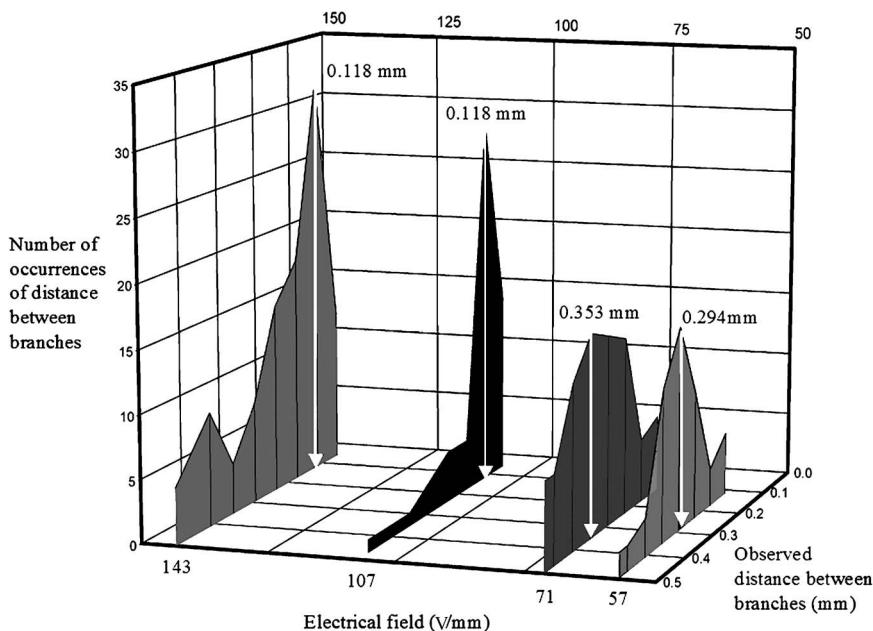
FIG. 3. Distributions of distances between the adjacent branches at different applied electric field (applied potential/gap distance). The distributions are broad at the lower electric fields, so the uncertainties in experimental values are large. The white arrows indicate the most frequently occurring distance between branches at each value of the electric field.

ing was perfectly periodic, the histogram at each electrical field would contain only one nonzero bin. As can be seen from Fig. 3, some much longer spaces were observed. The limited resolution of the optical images made accurate measurements of shorter spaces impractical, although shorter spaces were occasionally observed.

The significant spacing between branches at each voltage is considered to be the spacing associated with the highest peak in the histogram. The width of the highest peak is broadest at the lower electric fields. There is no evidence of branches forming and then breaking off at the root of the branch. Some branches are "missing" from the presumed periodic occurrence of the branches. Sometimes a weak "second-order peak" was observed in the histogram, with a spacing about twice as long as the spacing represented in the primary peak. The second-order peak suggests the occurrence of a nonlinear effect, with energy pumped from a leading mode to a following mode, in a way that is similar to the occurrence, in the capillary breakup of jets, of satellite droplets between the primary droplets.

Table I lists the experimental data for the four potential values used, in kilovolts. Each value of the potential is associated with an average excess charge per unit jet length and an electric field determined mainly by the potential applied and the radius of the jet. In electrospinning, both charge per unit length and the jet diameter change as the jet elongates and tapers.[3,4,12–14]

The linear theoretical model described below predicts

that the observed spacing is approximately related to the spacing between the radial maxima of the static equilibrium undulations on an infinitely long, nontapering liquid jet. This prediction does not rule out the possibility that the absence of branches at predicted locations may have other, perhaps nonlinear, causes.

Branching can be profuse, with many long, closely spaced, and rapidly growing branches. Jets with larger diameters, associated with higher voltages, tend to have more branches. As will be discussed after the theoretical model is described, when the diameter of the jet becomes larger at a higher voltage, the wavelength in the axial direction of the static undulations on the surface becomes shorter and the development of closely spaced branches is expected. The bending instability and the occurrence of branching coexist with only minor interactions, even when both instabilities are fully developed as in Fig. 4. The taper rates of the thinner jets with fewer branches cannot be determined accurately from the earlier figures, but it appears to be about a factor of 10 smaller than that shown in Fig. 4.

III. INTRODUCTION TO THEORY

An infinitely long jet of incompressible fluid with a uniform circular cross section is the theoretical model used as a starting point to describe a mechanism that leads to quasi-periodic branching of an electrospinning jet. Gravitational effects are negligibly small.[3] The electrical conductivity is large enough to assume that excess charge is always at the surface.

The surface of the jet can respond to the presence of the electrical Maxwell forces in the following interesting way. If any element of the charged surface moves outward in response to the electrical forces, the motion of that element will extract energy from the electrical field in order to form a "hill." The lateral surface area associated with the growing hill must increase because volume is conserved, since flow from the ends cannot occur in an infinitely long jet of incom-

TABLE I. The experimental results characterizing the branching.

φ_0 (kV)	Electric field (V/mm)	Number of observed branching events	Total observed numbers of distances between branches
4	57	6	68
5	71	5	91
7.5	107	2	54
10	143	5	108
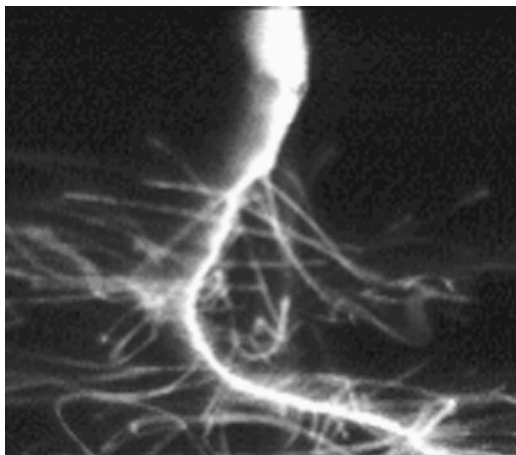
FIG. 4. A thick jet with many closely spaced branches and a high taper rate is shown. The diameter decreases between 1% and 2% per unit distance along the segment shown. The still images of PCL solution were taken by a high-speed camera at a frame rate of 2000 frames/s. Bending and branching began after only a short distance from the tip. The 15% PCL solution was electrospun with 10 kV, and gap distance from pipette to copper plate collector was 70 mm. The width of this frame is about 12 mm. The exposure time was 0.1 ms.

pressible fluid. The energy required to form the undulating surface of hills, saddle points, and valleys is provided by the electric field. The resulting static undulations may be quite complicated. The distribution of electrical charge on the surface of the jet is similarly complicated.

The liquid in the fluid jet is assumed to be a perfect electrical conductor, which means that the time intervals required for changes in the shape of the surface are much longer than the characteristic charge relaxation time τ_c. The relaxation time for PCL solutions in acetone can be estimated using the data from Ref. 15. There, in Table I the relative permittivity ε and the electric conductivity σ_e are given as $\varepsilon \approx 25.2$ and $\sigma_e \approx 0.142$ mS/m$=1.278 \times 10^6$ s^{-1}. Therefore, $\tau_c = \varepsilon/(4\pi\sigma_e) \approx 0.155 \times 10^{-2}$ ms. If the jet were a perfect nonconductor of electricity, the redistribution of charge on the surface that is required to stabilize an undulating surface by an intricate balance of electrical and surface tension forces might not be possible.

To find a mathematical expression for the undulating shapes, the solution of the partial differential equation that describes the shape of the surface of the jet and the electric field in the linear approximation is written as a two-dimensional Fourier series that depends on the azimuthal angle and the distance along the axis of the jet. Substituting the assumed Fourier series into the partial differential equation and using the boundary conditions to evaluate the coefficients of the various terms in the Fourier series leads to the identification of terms (also called modes in this paper) in the series that are in equilibrium, static, and nonzero. The sum of these nonzero modes determines the shape of the undulating surface of the jet. Since only a subset of the Fourier modes is static, there is a finite wavelength associated with the static mode that has the longest wavelength along the axis.

In the stability analysis that follows it is argued that the longest allowed static wavelength along the jet axis leads to the observed quasiregular spacing of the branches.

A smooth jet with a circular cross section is the only stable shape at low electrical potential differences. Not every undulating shape can occur in equilibrium as the potential is increased, but some static undulations of the jet surface inevitably occur. Near the highest peaks of the static undulations, shape perturbations, which increase the radius or the curvature, grow rapidly and give rise to branching.

It is shown that, if the amplitude of the static Fourier mode that has the longest wavelength is dominant and if the curvature near the higher peaks is high, it is likely that a branch will develop near each of the peaks of the longest wavelength Fourier mode. The condition for high curvature is likely to be satisfied almost everywhere by the presence of shorter wavelength Fourier modes with small amplitudes.

IV. THEORY OF EQUILIBRIUM STATIC UNDULATIONS ON THE JET

For spinnable polymer solutions, capillary breakup of the polymeric fluid jet into drops takes much longer than the time intervals required to establish an undulating surface on a jet.[16] The first question we address is can a steady-state, equilibrium, and noncircular cross-sectional shape of the fluid jet exist under the combined action of the surface tension and the electric Maxwell stresses? For simplicity we assume that the space between the fluid jet and the electrode is vacuum. The fluid is considered to be a perfect conductor. We also assume that the radial deviations from the circular cross-sectional shape are small and can be considered as small perturbations so that $\zeta \ll a$, where ζ is the undulation amplitude and a is the unperturbed cross-sectional radius. The experimental evidence in Figs. 2(a) and 4 shows that the jets we are dealing with are tapering (and may also be bending) in the length scale A of the order of several millimeters to 1 cm. The cross-sectional radius is $a \approx 10^{-2}$ cm. The detailed asymptotical analysis of the electric field about a slender tapering jet in the axial outer capacitor field is readily available.[17] It shows that the radial component of the electric field near the jet is given by $E_r = \varphi_0/[r \ln(A/a)]$, where φ_0 is the difference of the local potential of the jet surface and the local potential of the outer capacitor field (φ_0 is a slight function of the axial coordinate in the jet z). This is formally equivalent to the notion of a hollow cylindrical electrode with a large radius A, as sketched in Fig. 5. Note that an idea of such virtual hollow cylindrical electrodes can be traced back to Ref. 18. In Fig. 5 the radial axis and the azimuthal angle of the cylindrical frame of reference are also shown, and the axial coordinate z is perpendicular to the page.

In Fig. 5 the electrical potential of the jet is chosen as zero, although in many experimental situations the zero-potential "ground," represented here by the large cylinder, is chosen to be zero. The choice of the location of the zero potential is arbitrary, since only the difference in potential between the jet and the large cylinder (or ground) matters.

The measured wavelengths of the branching instability (the interbranching distances) discussed in detail in Sec. VI are of the order of $\lambda \approx 10^{-2}$ cm. The smallness of the ratio λ/A, which is of the order of 10^{-2}, allows the application of the local analysis of the electric and hydrodynamic fields, in
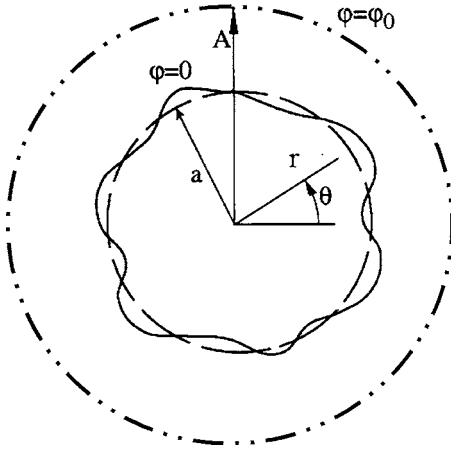
FIG. 5. Sketch of the cross section of the jet. The dashed line represents the surface of an unperturbed infinitely long cylindrical jet. The superimposed solid line represents a cross section of the jet corresponding to an arbitrarily chosen deviation from the original circular cross section. The existence of six radial undulations suggests that the Fourier mode with the azimuthal wave number $n=6$ is dominant for the configuration shown. The outer circle represents, at a different scale, the virtual hollow cylindrical electrode, which is assumed to have a radius A that is much larger than the radius of the jet a.

particular, to dispense with the slight dependence of φ_0 on z considering z as being a "frozen" parameter of the unperturbed state. When perturbations are considered, local analysis of tapering capillary jets in Refs. 19–22 shows that tapering would cease to affect the evolution of small perturbations at the distances of the order of 1 mm from the nozzle in our case. This means that almost all the perturbations and branches seen in Figs. 2(a) and 4 are practically unaffected by tapering.

In the local analysis we employ, the electric potential φ is subject to the Laplace equation

$$\frac{1}{r}\frac{\partial}{\partial r}\left(r\frac{\partial \varphi}{\partial r}\right) + \frac{1}{r^2}\frac{\partial^2 \varphi}{\partial \theta^2} + \frac{\partial^2 \varphi}{\partial z^2} = 0. \tag{1}$$

In the case of an unperturbed circular cross section the boundary conditions are

$$r = a, \quad \varphi = 0, \tag{2a}$$

$$r = A, \quad \varphi = \varphi_0. \tag{2b}$$

The solution is given by

$$\varphi = \varphi_0 \frac{\ln(r/a)}{\ln(A/a)}. \tag{3}$$

Beginning from the classical works of Rayleigh and Weber it is well known that the linear stability analysis of small perturbations accurately predicts the wavelength of the fastest growing mode of perturbations of free liquid jets.[16,23–25] The wavelength does not change much during the nonlinear stage. Therefore, the interbranching distances at the nonlinear stage are actually determined during the linear stage. One of our main goals is the prediction of the interbranching distances measured experimentally (cf. Figs. 2–4). To achieve that goal, large perturbation amplitudes are not required since the interbranching distances are determined in

the linear stage when perturbations are small.

In the static analysis of the present section in the general case a small radial undulation of the surface can be represented as

$$\zeta = \zeta_n e^{i[n\theta + k_n z]}, \tag{4}$$

where ζ_n is the amplitude, n is the azimuthal wave number, and $k_n = 2\pi/\lambda_n$ is the axial wave number with λ_n being the wavelength along the jet axis associated with a particular azimuthal wave number. Note that for small perturbations the perturbed cross-sectional area in Fig. 5 is automatically equal to the unperturbed one.

A solution of Eq. (1) is sought in the form

$$\varphi = \varphi_0\left[\frac{\ln(r/a)}{\ln(A/a)} + F(r)\zeta(\theta,z)\right]. \tag{5}$$

Substitution of Eq. (5) in Eq. (1) yields the modified Bessel equation with the solution

$$F(r) = C_1 I_n(kr) + C_2 K_n(kr), \tag{6}$$

where I_n and K_n are the modified Bessel functions, and the cases where $n \geq 2$ are relevant. The function $F(r)$ clearly depends on n, but it causes no confusion here to omit the subscript n. Also, we omit n in the notation of the axial wave number and here and hereinafter use k instead of k_n.

C_1 and C_2 are the constants of integration. They are found via the boundary conditions

$$r = a + \zeta, \quad \varphi = 0, \tag{7a}$$

$$r = A, \quad \varphi = \varphi_0. \tag{7b}$$

Using Eqs. (5)–(7) and linearizing for $\zeta \ll a$, we obtain

$$F(r) = \frac{K_n(kA)I_n(kr) - I_n(kA)K_n(kr)}{a\ln(A/a)[I_n(kA)K_n(ka) - I_n(ka)K_n(kA)]}. \tag{8}$$

The normal Maxwell stress associated with the electric field at the surface of the fluid jet is equal to $(\partial\varphi/\partial\perp)^2/8\pi$, where $(\partial/\partial\perp)$ denotes the derivative along the normal to the surface and Gaussian (cgs) units are used. Linearizing, we obtain the electrical normal stress outside the jet surface in the form of a component of a second-rank tensor[26]

$$\sigma_{\perp\perp}^{\text{outside}} = \frac{\varphi_0^2}{8\pi}\left[\frac{1}{a^2\ln^2(A/a)} - \frac{2\zeta}{a^3\ln^2(A/a)}\right.$$
$$\left. + \frac{2(dF/dr)|_{r=a}\zeta}{a\ln(A/a)}\right]. \tag{9}$$

The second and third terms inside the square brackets of Eq. (9) are referred to later as the perturbed part of the pressure. In the equilibrium state considered in the present section, pressure inside the fluid jet is constant (C), so that the normal stress inside the jet is

$$\sigma_{\perp\perp}^{\text{inside}} = -C. \tag{10}$$

The pressure difference (p_γ) between $\sigma_{\perp\perp}^{\text{outside}}$ and $\sigma_{\perp\perp}^{\text{inside}}$ is due to the capillary pressure associated with the surface tension (γ),

$$p_\gamma = \gamma\left[\frac{1}{a} - \frac{1}{a^2}\left(\zeta + \frac{\partial^2\zeta}{\partial\theta^2}\right) - \frac{\partial^2\zeta}{\partial z^2}\right]. \qquad (11)$$

The expression for p_γ has been simplified since $\zeta \ll a$. At the surface of the fluid jet the boundary condition is

$$\sigma_{\perp\perp}^{\text{inside}} = \sigma_{\perp\perp}^{\text{outside}} - p_\gamma. \qquad (12)$$

Note that in static cases considered in the present section the velocity is zero and thus all the viscous stresses are zero in Eq. (12).

As a convention, pressure is usually thought of as positive inside a droplet and outwardly directed stress is considered to be a negative pressure. Equation (12) means, as usual, that pressure inside is equal to the pressure outside plus the pressure associated with surface tension. Substituting Eqs. (9)–(11) into (12), we separate first the unperturbed part, which yields the dimensional constant C as shown in Eq. (13)

$$C = \frac{\gamma}{a} - \frac{\varphi_0^2}{8\pi a^2 \ln^2(A/a)}. \qquad (13)$$

The stress acting on the surface of the fluid from the outside is due to the electrical Maxwell stress defined in Eq. (9) and discussed near Eq. (13) of Ref. 27. The perturbed electric forces are associated with the redistributed electric charge at the surface of a perturbed jet. Also, according to the perturbed part of Eq. (12), the perturbed part of the stress from inside the jet comes from the perturbed part of the Maxwell stress and the capillary pressure. To have perturbed pressure in an incompressible fluid in a jet with a more complicated static shape, it is necessary to require equality between the perturbed electrical forces and the perturbed capillary pressure everywhere on the complicated static shape. The separated perturbed part of Eq. (12), after some algebra, yields the following equation:

$$D = \frac{(1 - n^2 - \chi^2)\ln^2 \bar{A}}{\Phi(\chi, n, \bar{A})}, \qquad (14)$$

here D and χ are both dimensionless and the following notation is used:

$$\chi = ka \text{ and } n \geq 2 \qquad (15a)$$

$$\bar{A} = A/a > 1, \qquad (15b)$$

$$D = \frac{\varphi_0^2}{4\pi\gamma a}, \qquad (15c)$$

$$\Phi(\chi, n, \bar{A})$$
$$= 1 - \chi\left\{\frac{K_n(\chi\bar{A})[dI_n(\chi)/d\chi] - I_n(\chi\bar{A})[dK_n(\chi)/d\chi]}{I_n(\chi\bar{A})K_n(\chi) - I_n(\chi)K_n(\chi\bar{A})}\right\}. \qquad (15d)$$

Equation (14) reduces to

$$D = \frac{(1 - n^2)\ln^2 \bar{A}}{1 - n(\bar{A}^n + \bar{A}^{-n})/(\bar{A}^n - \bar{A}^{-n})} \qquad (16)$$

as $\chi \to 0$. In the most relevant case where $\bar{A} \gg 1$, Eq. (16) can be further simplified and takes the form

$$D = (1 + n)\ln^2 \bar{A}, \qquad (17)$$

which approximately yields

$$D = n\ln^2 \bar{A}, \qquad (18)$$

since as we shall see in Sec. VI, the values of $n = 7 - 9$ are of interest in the present case. As $\chi \to \infty$ Eq. (14) reduces to

$$D = \chi\ln^2 \bar{A}. \qquad (19)$$

When Eq. (14) has a solution for a given potential φ_0 and n (or, equivalently, a given D and n), a nontrivial static equilibrium shape of the jet surface that undulates both in azimuthal directions and along the axis is possible. The solution of Eq. (14) yields a dimensionless longitudinal wave number χ_n corresponding to each value of n (the azimuthal wave number) for which the solution exists. Then the superposition of the azimuthal and axial modes, corresponding to each value of n for which a solution exists, is the calculated equilibrium shape of the jet surface written as

$$\bar{r}_{\text{surface}} = 1 + \sum_{n=2}^{N} \bar{\zeta}_n \cos(n\theta + \chi_n\bar{z}), \qquad (20)$$

where $\bar{\zeta}_n$ is the amplitude of the nth mode of the Fourier series that represents deviations from a smooth cylindrical shape of the jet surface divided by a to make the amplitude dimensionless. Similarly $\bar{r}_{\text{surface}}$, and $\bar{z}$ are obtained by dividing r_{surface} and z by a. N is the largest value of n for which a solution of Eq. (14) exists. Based on the stability considerations in Sec. V, we suggest that the Fourier mode, labeled by N, in expression (20) for $\bar{r}_{\text{surface}}$ plays a major role in the establishment of the spacing between the branches and provide experimental data that support the reasonableness of this suggestion. A similar calculation is described in Ref. 28 where a planar unperturbed liquid surface and a planar electrode parallel to it were considered. The present calculation differs from that of Ref. 28 in an important aspect. The planar surface under the finite electrode considered in Ref. 28 can rise uniformly without developing any undulations because, at the edges, fluid can flow under the electrode. In our description of the behavior of an infinitely long cylinder, the volume of the fluid inside the jet is conserved. Flow of additional liquid into the jet from the ends, which are at an infinite distance, is not considered. Therefore, development of radial undulations on the surface of a cylinder must occur on the unperturbed cylindrical surface and not on the background of a uniform increase in the radius of the jet, which would be analogous to the rise of the free surface under the finite electrode in planar case.[28]

Equation (14) was solved numerically and the results are depicted in Fig. 6, which is a graph of D as a function of χ. A solution is identified by the intersection of the straight horizontal line corresponding to a particular value of the di-
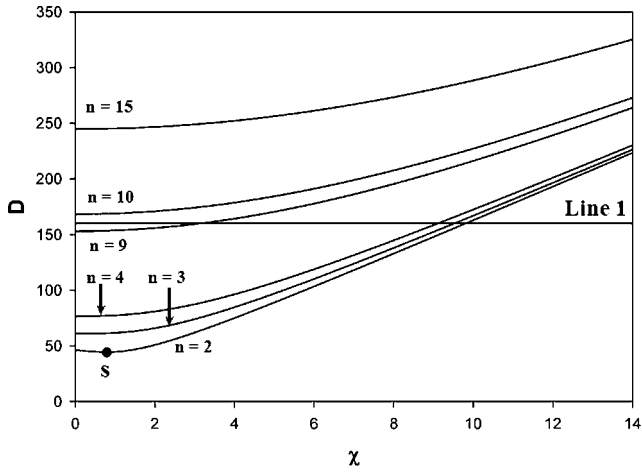
FIG. 6. The straight "line 1" shows the value of D for $\varphi_0 = 5$ kV. The curve $n=2$ has its lowest value at the point S, which corresponds to the onset of branching. This corresponds to the lowest value of D at which stable undulations can occur. No branching is predicted at lower values of the dimensionless potential D. Also, for the chosen value of $\varphi_0 = 5$ kV, modes with $n>9$ yield no solutions. Hence, $N=9$ in this case.

mensionless parameter D, with the curves representing the value of the right-hand side of Eq. (14) as a function of χ. Figure 6 will also be discussed in more detail in Sec. V in the context of the stability analysis and comparison with experimental data.

V. RELATIVE STABILITY OF PERTURBATIONS OF THE CIRCULAR CROSS-SECTIONAL SHAPE

As the potential is increased, the cylindrical jet can develop complicated undulations that are stable in time. Due to further perturbations, the undulations change in shape and can become unstable and grow with time.

The stability problem is considered here. A flow inside the jet, which follows the development of undulations on the surface, is allowed. This flow is described in the frame of reference associated with the jet in flight. Such a flow is

governed by the linearized Navier-Stokes equations[23,29–31] in cylindrical coordinates with the following linearized boundary conditions imposed at the jet surface (where in the linear approximation $r=a$):

$$v_r' = \frac{\partial \zeta}{\partial t}, \tag{21a}$$

$$\sigma_{r\theta}' = 0, \tag{21b}$$

$$\sigma_{rz}' = 0, \tag{21c}$$

$$-\sigma_{rr}' = -\frac{\gamma}{a^2}\left(\zeta + \frac{\partial^2 \zeta}{\partial \theta^2}\right) - \gamma\frac{\partial^2 \zeta}{\partial z^2} - \frac{\varphi_0^2}{8\pi}\left[-\frac{2\zeta}{a^3 \ln^2 \bar{A}}\right.$$
$$\left. + \frac{2(dF/dr)|_{r=a}\zeta}{a \ln \bar{A}}\right]. \tag{21d}$$

The primes indicate small perturbations of the named functions.

Equation (21a) is the kinematical boundary condition relating the perturbed radial component of velocity to perturbations of the undulation amplitude ζ, with t being the time. Conditions (21b) and (21c) imply the absence of viscous shear stresses at the jet surface. The last boundary condition (21d) corresponds to the balance of normal stresses at the jet surface and is a generalization of Eq. (12) for the dynamic case. Note that the perturbed radial stress σ_{rr}' incorporates the viscous stresses at the jet surface. Equations (9) and (11) were also used. Subscripts r, θ, and z correspond to the radial, azimuthal, and axial directions of the cylindrical coordinate system associated with the moving jet. All the perturbations we are introducing now incorporate the factor $\exp[\delta t + i(n\theta + k_n z)]$, with δ being the growth rate [cf. with the static Eq. (4)]. After solving the linearized Navier-Stokes equations and satisfying the boundary conditions (21), we arrive at the following dimensionless characteristic equation of the problem which determines the growth rate δ

$$\bar{\delta}^2 + \bar{\delta}\mathrm{Oh}^2\frac{\chi}{I_n(\chi)}\{W(\chi,\xi)\xi I_{n+1}'(\xi) + U(\chi,\xi)\xi I_{n-1}'(\xi) + \chi[I_{n+1}'(\chi) + I_{n-1}'(\chi)]\}$$
$$= \mathrm{Oh}^2\frac{\chi}{I_n(\chi)}\left[1 - s^2 + \frac{D}{\ln^2 \bar{A}}(\chi T - 1) - \chi^2\right] \times \frac{1}{2}\{W(\chi,\xi)I_{n+1}(\xi) + U(\chi,\xi)I_{n-1}(\xi) + I_{n+1}(\chi) + I_{n-1}(\chi)\}. \tag{22}$$

Some details of the calculations leading to Eq. (22) can be found in Ref. 30 where viscous Newtonian fluids were considered and in Ref. 31 where viscoelastic Maxwell fluids were considered. In the present work we obtain the Newtonian case as the limiting case, with the Deborah number zero, of the results of Ref. 31. Some comparisons are made with Ref. 30 as well. The following notations are adopted in Eq. (22) for the dimensionless perturbation growth rate $\bar{\delta}$, the dimensionless Ohnesorge number (Oh) that characterizes the

ratio of the viscous to the inertial and surface tension forces, and the dimensionless parameter ξ:

$$\bar{\delta} = \frac{\delta \mu a}{\gamma}, \tag{23a}$$

$$\mathrm{Oh} = \frac{\mu}{(\rho\gamma a)^{1/2}}, \tag{23b}$$

$$\xi^2 = \chi^2\left(1 + \frac{\bar{\delta}}{\chi^2}\frac{1}{\text{Oh}^2}\right). \tag{23c}$$

The viscosity is denoted by μ. For convenience, functions $W(\chi,\xi)$ and $U(\chi,\xi)$ used in Eq. (22) are given in the Appendix. Also, the expression for T in Eq. (22) is

$$T = \frac{K_n(\chi\bar{A})dI_n(\chi)/d\chi - I_n(\chi\bar{A})dK_n(\chi)/d\chi}{I_n(\chi\bar{A})K_n(\chi) - I_n(\chi)K_n(\chi\bar{A})}. \tag{24}$$

It is emphasized that Eq. (22) is valid for $n \geqslant 0$, i.e., for the circular cross section ($n=0$), for the bending ($n=1$), and for the branching ($n \geqslant 2$) modes. In the case of electrospinning, viscous forces in the polymer solution dominate the dynamics of small perturbations of the shape of thin jets, and surface tension is less significant.

When the viscous forces dominate the surface tension, the Ohnesorge number is much greater than 1, $\text{Oh} \gg 1$.

The circular cross-section case ($n=0$) with and without an electric field was studied in the seminal works of Rayleigh,[24] Weber,[25] and Chandrasekhar.[23] In this ($n=0$) case, for $\text{Oh}^2 \gg 1$, Eq. (23c) can be approximated as

$$\xi = \chi\left(1 + \frac{\bar{\delta}}{2\chi^2}\frac{1}{\text{Oh}^2}\right). \tag{25}$$

In addition, for $n=0$ and for any χ, one can obtain from Eqs. (A1)–(A8) in the Appendix that

$$W(\chi,\chi) = U(\chi,\chi) = -1. \tag{26}$$

Given Eqs. (25) and (26), both factors in the curly brackets in Eq. (22) are expected to be the order of $\mathcal{O}(1/\text{Oh}^2)$, whereas the terms in Eq. (22) are actually of the order $\mathcal{O}(1)$. In this case no terms disappear in Eq. (22) in spite of the limit of large Ohnesorge number. The resulting equation contains $\bar{\delta}$ as a factor in all the terms. This $\bar{\delta}$ is cancelled from each term, and a linear equation for $\bar{\delta}$ yields the solution of Rayleigh,[24] Weber,[25] and Chandrasekhar[23] given by Eq. (19) in Ref. 30. Note that in Ref. 30, as in this paper, the case of $\bar{A} \gg 1$ was considered. Without the electric field the result of Rayleigh,[24] Weber,[25] and Chandrasekhar[23] just mentioned, corresponds to the capillary instability of very viscous fluid jets. Weber[25] also showed that the characteristic equation for the pure capillary instability (with no electric effects involved) of highly viscous jets is very accurately approximated by the following long-wave limit formally valid for $\chi \to 0$:

$$\bar{\delta} = \frac{1}{6}(1 - \chi^2). \tag{27}$$

The case of $n=1$ corresponds to the bending instability and, in fact, has already been studied in the long-wave approximation in Refs. 3 and 4. In the case we are dealing with in the present work, for $n \geqslant 2$, the factors in the curly brackets in Eq. (22) are of the order of $\mathcal{O}(1)$, and not of the order of $\mathcal{O}(1/\text{Oh}^2)$ as it was for $n=0$. Therefore, in Eq. (22) in the case of $\text{Oh}^2 \gg 1$, the dominant terms are those which contain the multiplier Oh^2 (specifically the second term on the left-hand side and the term on the right-hand side). Then the $\bar{\delta}^2$

term can be neglected. The solution of the characteristic equation (22) for the case of interest $n \geqslant 2$ becomes

$$\bar{\delta} = \frac{1}{2}\left[1 - n^2 + \frac{D}{\ln^2 \bar{A}}(\chi T - 1) - \chi^2\right]Y(\chi), \tag{28}$$

where Y is the function defined for convenience as

$$Y(\chi)$$
$$= \frac{W(\chi,\chi)I_{n+1}(\chi) + U(\chi,\chi)I_{n-1}(\chi) + I_{n+1}(\chi) + I_{n-1}(\chi)}{\chi[W(\chi,\chi)I'_{n+1}(\chi) + U(\chi,\chi)I'_{n-1}(\chi) + I'_{n+1}(\chi) + I'_{n-1}(\chi)]}. \tag{29}$$

For $n \gg 1$ and $\chi \to 0$

$$Y(\chi) = \frac{1}{n}. \tag{30}$$

Note that Eqs. (28)–(30) of the present work yield the same asymptotical behavior as the asymptotical behavior following from Eq. 22 of Ref. 30 when $\bar{A} \gg 1$, $n \gg 1$, and $\chi \to 0$. On the other hand, for $\chi \to \infty$,

$$Y(\chi) = \frac{1}{\chi}. \tag{31}$$

Also note that $Y(\chi) > 0$ for any $0 \leqslant \chi \leqslant \infty$. Therefore, the sign of $\bar{\delta}$ given by Eq. (28) is fully determined by the factor in the square brackets in Eq. (28). Then the threshold to the instability occurs when the term in the square brackets in Eq. (28) becomes equal to zero, which yields Eq. (14). The onset of branching instability is indicated when, for any allowed n, the dimensionless wave number χ belongs to the range $0 \leqslant \chi \leqslant \chi_n$, where χ_n is a solution of Eq. (14). For this range of χ, Eq. (28) yields $\bar{\delta} > 0$, which indicates the onset of instability.

VI. RESULTS AND DISCUSSION

We now examine the stability of the individual modes, which add together to describe the static undulations as the potential is increased, to show that perturbations of the undulation amplitude ζ in regions near the highest peaks, with the highest curvature, will grow most rapidly. In the calculations, the value of $\bar{A}=50$ was used, which yields a plausible value of A of the order of $2500-4750$ μm for the values of a listed below. The results of the calculations change only slightly when $\bar{A}$ is varied by 20%. The following four cases, for which the experimental information has been described above, were considered:

TABLE II. The wavelengths of the static undulations λ_n predicted in case (ii), $\varphi_0=5$ kV.

n	χ_n	λ_n (calculated) (μm)
2	9.81	38.4
3	9.53	39.6
4	9.11	41.3
5	8.55	44.1
6	7.81	48.3
7	6.81	55.3
8	5.43	69.4
9	3.17	119.0

(i) $\varphi_0=4$ kV, $a=50$ μm;
(ii) $\varphi_0=5$ kV, $a=60$ μm;
(iii) $\varphi_0=7.5$ kV, $a=95$ μm; and
(iv) $\varphi_0=10$ kV, $a=95$ μm.

In the calculations we used $\rho=791$ kg/m^3 and $\gamma=23$ mN/m for the PCL dissolved in acetone. A representative situation is depicted in Fig. 6 corresponding to case (ii). Here there are intersections of line 1 representing (D) with curves that show the value of the right-hand side of Eq. (14) for several values of n. The allowed modes, the corresponding wave numbers in the axial direction χ_n, and wavelengths along the axis ($\lambda_n=2\pi a/\chi_n$) are shown in Table II. In this case, with $\varphi_0=5$ kV, solutions of Eq. (14) exist for values of n from 2 to 9, where the intersections of the straight line 1 with the curves $D(\chi)$ occur. The longest wavelength has the subscript $N=9$ and λ_9 is equal to 119 μm. The curves for $n=10$ and for $n>10$, e.g., $n=15$, do not intersect line 1, so static equilibrium solutions exist only for $\chi_2-\chi_9$. The smallest value of χ_n, (called χ_N) corresponds to the mode with the longest wavelength that is allowed, which is called λ_N.

To illustrate the predicted static equilibrium undulations that occur under these experimental conditions, namely, to predict their "landscape," it is necessary to assume their amplitudes and phases. Since the experimental observation does not provide these amplitudes, we illustrate the calculation by assuming that only two modes have nonzero amplitudes. The assumed amplitudes of the modes are $\bar{\zeta}_2=0.03$, $\bar{\zeta}_3=\cdots=\bar{\zeta}_8=0$, and $\bar{\zeta}_9=0.1$. The phases of all the modes are set to zero at $z=0$ in this example. Note that the distance between the branches is dominated by the longest allowed wavelength along the axis λ_N which is not affected by the amplitudes and phases of the modes.

The fluid jet cross section (the xy plane at $z=0$) with equilibrium static undulations corresponding to $\varphi_0=5$ kV [case (ii)] is shown by the heavy line in Fig. 7. The median longitudinal section of the fluid jet for this case is shown as the heavy line in Fig. 8. As the potential difference increases, the static equilibrium shapes of the fluid jet become more complicated with higher modes involved. For $\varphi_0=4$ and 10 kV, for example, $N=7$ and 25, respectively. Table III lists the values of N predicted for the four cases considered. The three-dimensional shape of the surface of the fluid jet corresponding to that of Figs. 7 and 8, case (ii) with $\varphi_0=5$ kV, is depicted in Fig. 9.
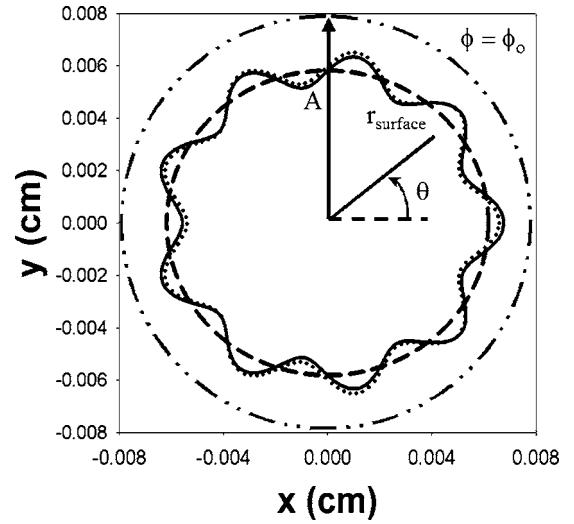
FIG. 7. The solid line shows cross-sectional shape at $z=0$ in case (ii). The shape corresponds to an arbitrary choice of $\bar{\zeta}_2=0.03$ and $\bar{\zeta}_9=0.1$ and $\bar{\zeta}_n=0$ for $n=3-8$; $a=0.006$ cm. The resulting cross-sectional shape is obviously noncircular. The dashed line shows the shape of the cross section resulting from a single mode with $\bar{\zeta}_2=0.03$ and $\bar{\zeta}_3-\bar{\zeta}_9=0$, the dotted line shows the cross section for $\bar{\zeta}_9=0.1$ and $\bar{\zeta}_2-\bar{\zeta}_8=0$. The radius ($A$) of the double dots and dash ($\cdots$—$\cdot$—) circle representing the virtual outer electrode was reduced by an appropriate factor to fit in the frame of this diagram. The radius to a point on any surface of interest is $r_{surface}$.

The curvature (K in cm^{-1}) at any (θ,z) position on the undulating, static, and equilibrium surface is readily calculated from Eq. (20). For case (ii) with $\bar{\zeta}_2=0.03$ and $\bar{\zeta}_9=0.1$ and $\bar{\zeta}_n=0$ for $n=3-8$ considered here, the curvature is

$$K = (1/a)[1 + 0.03(3 + \chi_2^2)\cos(2\theta + 2\pi z/\lambda_2) + 0.1(80 + \chi_9^2)\cos(9\theta + 2\pi z/\lambda_9)], \qquad (32)$$

where a, z, λ_2, and λ_9 are all measured in centimeters.
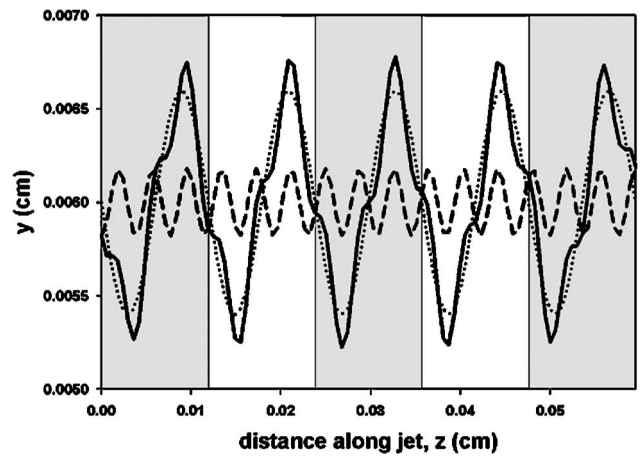
FIG. 8. The calculated longitudinal section at $x=0$ of the surface of the fluid jet in case (ii) with $\bar{\zeta}_2=0.03$ and $\bar{\zeta}_9=0.1$ and $\bar{\zeta}_n=0$ for $n=3-8$ is shown by the solid line. The dashed line shows the shape of the cross section resulting from a single mode with $\bar{\zeta}_2=0.03$ and $\bar{\zeta}_3-\bar{\zeta}_9=0$. The dotted line shows the cross section for $\bar{\zeta}_9=0.1$ and $\bar{\zeta}_2-\bar{\zeta}_8=0$. For the latter two curves according to Table II the wavelengths are $\lambda_2=38.4$ μm and $\lambda_9=119$ μm, respectively. The wavelength λ_9 is emphasized by shading the first, third, and fifth cycles. The same cycles are emphasized in Fig. 9.

TABLE III. The predicted number of static modes.

φ_0 (kV)	N
4	7
5	9
7.5	13
10	25

The upper part of Fig. 9 shows that the four points with the highest curvatures occur at irregular intervals along the z axis commensurate with the observed spacing of branches. The highest curvatures corresponded to an undulation with a radius of curvature of about $(1/2160)$ cm, which is about 4.63 μm.

The following stability analysis shows how this curvature pattern is related to the branching process. For the case (ii) φ_0=5 kV, a=60 μm, the growth rates of perturbations, predicted by Eqs. (28)–(31), for the Fourier modes with n =7, 8, and 9 are shown in Fig. 10.

The horizontal straight line in Fig. 10 represents $\bar{\delta}$=0. The static equilibria discussed above correspond to the intersection of this line with the curves for n=7, 8, and 9. The sections of the curves with $\bar{\delta}$>0 correspond to the instabil-
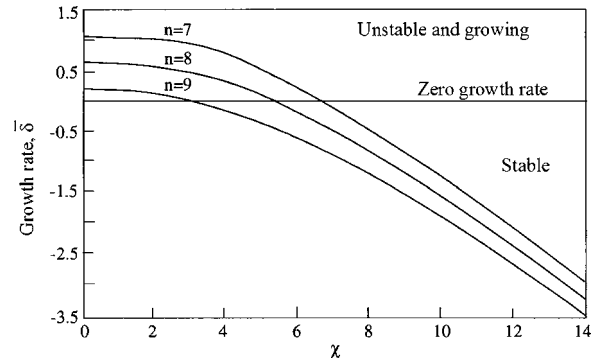
FIG. 10. Growth rates vs axial wave number for the modes along the axis that correspond to the azimuthal wave numbers n=7, 8, and 9. For those χ where $\bar{\delta}$>0, the instability sets in and perturbations amplitudes grow. This occurs for $0<\chi<\chi_n$, where χ_n correspond to static undulations.

ity, whereas with $\bar{\delta}$<0, to stability. Therefore, where a curve for a particular value of n is greater than zero, the corresponding perturbation will grow and the surface undulations are unstable. Where the curve is below zero, the corresponding perturbations will shrink. In Fig. 10 it is seen that for 0 $\leq\chi\leq\chi_n$ (the corresponding χ_n are given in the last three lines of Table II), perturbations amplitudes grow since $\bar{\delta}$
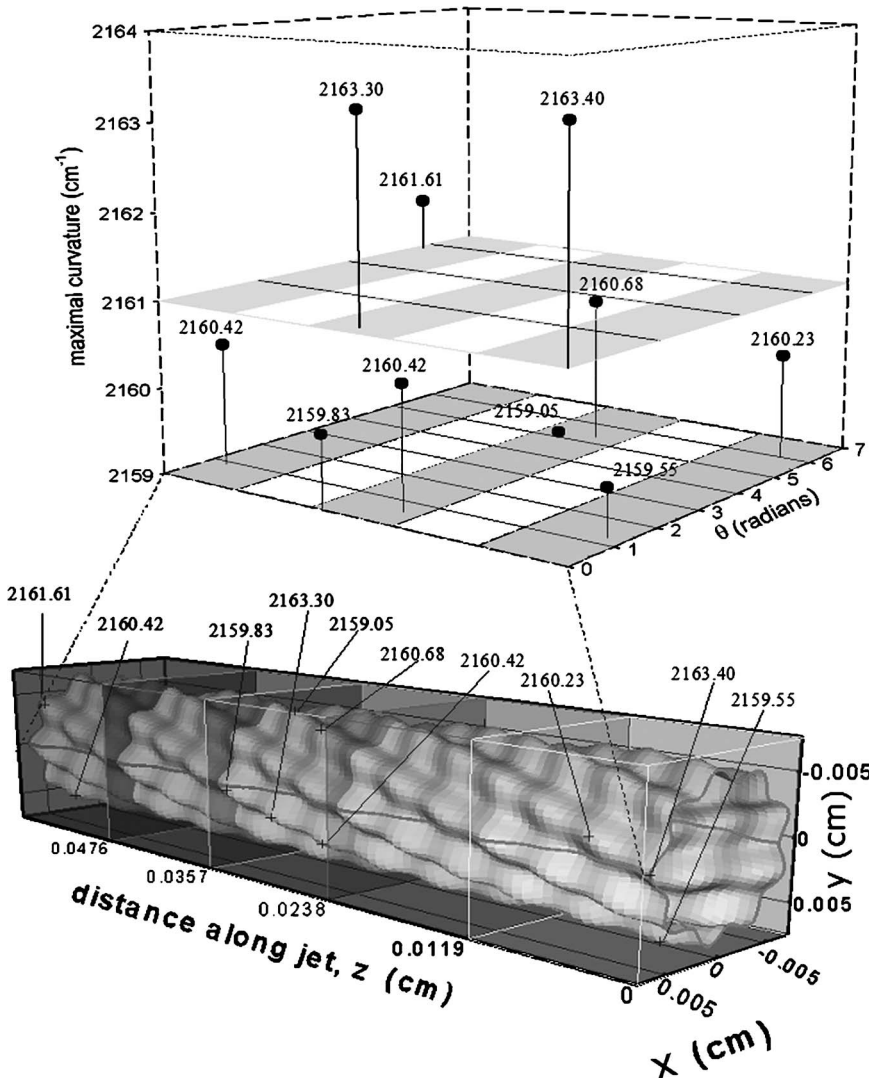
FIG. 9. The lower part shows a shaded perspective drawing of five cycles of the longest wavelength mode on the calculated surface of the jet for φ_0 =5 kV, case (ii), with $\bar{\zeta}_2$=0.03 and $\bar{\zeta}_9$=0.1 and $\bar{\zeta}_n$=0 for n=3–8. Each cycle is equal to λ_9 in length. The maximum curvatures in the cross sections along the jet were also calculated and values of the highest curvatures were plotted on the "unrolled" θz surface in the upper part of the figure. The locations of the highest curvatures of the surface are identified by arrows in the shaded drawing. In the θz planes for curvatures of 2159 and 2161 cm^{-1}, successive cycles are alternately shaded and unshaded for comparison with Fig. 8.

>0. The onset of the instability of undulation amplitude depends on the presence and amplitude of the electric field, since without an electric field $(D=0)$, $\bar{\delta}$ is always negative for any $n \geq 1$ according to Eq. (28).

The complicated static undulations of the surface, similar to the representative ones shown in Fig. 9, and corresponding only to the modes χ_n where $n=2-N$ could also be perturbed more by growing perturbations of modes with $\chi < \chi_n$. This is, in fact, inevitable and leads to radial growth in the neighborhood of the regions with the highest static curvature on peaks. The points with the highest static curvature occur at the peaks of the mode with $n=N$, i.e., $n=9$ in case (ii). Therefore, the undulations with χ close to χ_N i.e., $\chi \lesssim \chi_n$, actually develop the highest perturbation amplitude at the earliest time. Regions having the largest initial local curvature, which are located on the highest peaks, will grow most rapidly and give birth to branches. This is a consequence of the facts that $\bar{\delta} = \mathcal{O}(1)$ for all the modes and that there is no sharp maximum in the growth rate for any specific wave number, as shown by the curves for $n=7-9$ in Fig. 10. Therefore, the distance between the branches on the jet will be very close to the distance corresponding to χ_N for any given electric field and, in fact, determined by a static mode with $n=N$. Branching will happen first of all at a static crest with the highest curvature, which sits near the radial maxima of the mode with the wavelength $\lambda_N = 2\pi a / \chi_N$, as calculated from Eq. (14). Note that the values of $\bar{\delta}$ predicted for nonaxisymmetric electrically driven Fourier modes with $n \geq 2$ are larger or of the same order as for the axisymmetric perturbations of undulation amplitude with $n=0$ that lead to capillary instability. Indeed, for the capillary instability (where $n=0$) according to Eq. (27), the highest growth rate is $\bar{\delta}_{max} = 1/6$. However, the initial amplitudes of the nonaxisymmetric perturbations, which can lead to branching, add to the static undulations that already exist on the jet surface. These perturbations will grow even more rapidly than if they simply added to the radius of the cylindrical surface. Also note that in electrospinning, viscoelastic forces developed by the rapid elongation of the jets tend to prevent capillary breakup of both the primary and secondary jets. This is an additional stabilization produced by the nonlinear viscoelasticity due to polymer molecules.

According to the above discussion, each cycle of λ_N along the axis contains a region of high curvature near its peak, which can grow rapidly and become a branch. The spacing between these branches is of the order of λ_N [λ_9 in case (ii)]. This result is only slightly sensitive to the amplitudes $\bar{\zeta}_n$ assumed for the static undulations as long as the amplitude $\bar{\zeta}_N$ is the largest. These amplitudes are not observed in the experiment at present but, in principle, can be measured in the future. If the undulation amplitudes are as much as 1% of the radius of the jet, i.e., about 0.5 μm, it is possible that they might be seen. Interferences between light that passed through a cylindrical jet with light reflected from the surface of the same jet may provide a way to observe the presence of undulations of the surface.[32]

Experimental data on the spacing between branches are available for the four cases (i)–(iv), where the unperturbed

TABLE IV. The calculated and observed distances between branches along the jet.

Applied voltage (kV)	Average electric field between the tip and the collector (V/mm)	λ_N (calculated) (μm)	λ_N (measured) (μm)
4	57	379	294
5	71	119	353
7.5	107	118	118
10	143	124	118

jet radius was $50 \leq a \leq 95$ μm (cf. Fig. 3). Branching was observed in all four cases, with the branches being ≤ 10 μm in diameter. The calculations also indicated that branching could occur.

The calculations were made for all four potentials for which measurements are available, and the predicted branch spacings are compared with the measured ones in Table IV. The predictions at the higher voltage values (7.5 and 10 kV) are commensurate with the measurements. The comparison at the lower voltage values is not so good especially at 5 kV. The wide distribution of observed spacings at the lower voltage values shown in Fig. 3 may be caused by variations (perhaps a factor of 2) due to the elongation of the distance between branches that occurs after the branches start to grow. The experimentally observed spacing distributions at 7.5 and 10 kV suggest narrower distributions of the distance between branches, but the distances shorter than 100 μm between the branches could not be resolved in these optical images.

VII. SUMMARY AND CONCLUSIONS

Electrospinning of 15 wt. % polycaprolactone in acetone at voltage of $4-10$ kV and distances between electrodes of the order of several centimeters was accompanied by the emanation of a series of secondary jets in radial directions from the primary jet. The primary jet experienced, as usual, bending instability. Branching jets appeared at both straight and bending parts of the primary jet. An electrohydrodynamical theory proposed to describe this phenomenon showed that the surface of a conducting fluid jet can acquire complicated static equilibrium undulations under the combined effects of the electric Maxwell stresses and surface tension as the electrical stresses increase. A perfectly smooth cylindrical jet develops static undulations with complex shapes in a cylindrical electric field. It was shown that such undulating surfaces could become unstable at the sites of the highest local surface curvature on the tops of the longest wavelength undulations. This instability leads to the emanation of lateral branches from the primary jet at these unstable sites.

The observed and predicted distances between branches are commensurate for electrical potentials ranging from $4-10$ kV but the agreement is less than conclusive. At high voltages the distances between closely spaced branches were too small to be measured precisely and at low voltage the variation of the measured distance between branches was large. It was noted that both the experiment and the theory

show that as the applied voltage increases, the predicted distance between branches mostly decreases. An important future experimental problem is to observe the evolution of the undulations of the jet surface prior to the appearance of the branch jets.

ACKNOWLEDGMENTS

APPENDIX

$$S_1 = \{I_{n-1}(\chi) - I_{n+1}(\chi) + \chi[I'_{n+1}(\chi) - I'_{n-1}(\chi)] - n[I_{n+1}(\chi) + I_{n-1}(\chi)]\}, \tag{A1}$$

$$S_2 = \{I_{n-1}(\xi)[\xi^2 + (n-1)^2 + \chi^2 - 1] - n[-I_{n-1}(\xi) + \xi I'_{n-1}(\xi)]\}, \tag{A2}$$

$$S_3 = (-I_{n+1}(\chi)[2\chi^2 + (n+1)^2 - 1] - I_{n-1}(\chi)[2\chi^2 + (n-1)^2 - 1] + n\{[I_{n+1}(\chi) - I_{n-1}(\chi)] - \chi[I'_{n+1}(\chi) - I'_{n-1}(\chi)]\}), \tag{A3}$$

$$S_4 = [-I_{n-1}(\xi) + \xi I'_{n-1}(\xi) + n I_{n-1}(\xi)], \tag{A4}$$

$$S_5 = [I_{n+1}(\xi) - \xi I'_{n+1}(\xi) + n I_{n+1}(\xi)]\{I_{n-1}(\xi) \times [\xi^2 + (n-1)^2 + \chi^2 - 1] - n[-I_{n-1}(\xi) + \xi I'_{n-1}(\xi)]\} - [-I_{n-1}(\xi) + \xi I'_{n-1}(\xi) + n I_{n-1}(\xi)]\{I_{n+1}(\xi) \times [\xi^2 + (n+1)^2 + \chi^2 - 1] - n[I_{n+1}(\xi) - \xi I'_{n+1}(\xi)]\}, \tag{A5}$$

$$W(\chi,\xi) = \frac{S_1 S_2 - S_3 S_4}{S_5}, \tag{A6}$$

$$S_6 = [I_{n+1}(\xi) - \xi I'_{n+1}(\xi) + n I_{n+1}(\xi)],$$

$$S_7 = \{I_{n+1}(\xi)[\xi^2 + (n+1)^2 + \chi^2 - 1] - n[I_{n+1}(\xi) - \xi I'_{n+1}(\xi)]\}, \tag{A7}$$

$$U(\chi,\xi) = \frac{S_6 S_3 - S_1 S_7}{S_5}. \tag{A8}$$

[1] P. K. Baumgarten, J. Colloid Interface Sci. **36**, 71 (1971).
[2] D. H. Reneker and I. Chun, Nanotechnology **7**, 216 (1996).
[3] D. H. Reneker, A. L. Yarin, H. Fong, and S. Koombhongse, J. Appl. Phys. **87**, 4531 (2000).
[4] A. L. Yarin, S. Koombhongse, and D. H. Reneker, J. Appl. Phys. **89**, 3018 (2001).
[5] A. Theron, E. Zussman, and A. L. Yarin, Nanotechnology **12**, 384 (2001).
[6] E. Zussman, A. Theron, and A. L. Yarin, Appl. Phys. Lett. **82**, 973 (2003).
[7] A. G. MacDiarmid, Angew. Chem., Int. Ed. **40**, 2581 (2001).
[8] I. D. Norris, M. M. Shaker, F. K. Ko, and A. G. MacDiarmid, Synth. Met. **114**, 109 (2000).
[9] A. G. MacDiarmid *et al.*, Synth. Met. **119**, 27 (2001).
[10] S. Koombhongse, W. Liu, and D. H. Reneker, J. Polym. Sci., Part B: Polym. Phys. **39**, 2598 (2001).
[11] D. H. Reneker, W. Kataphinan, A. Theron, E. Zussman, and A. L. Yarin, Polymer **43**, 6785 (2002).
[12] A. F. Spivak and Y. A. Dzenis, J. Appl. Mech. **66**, 1026 (1999).
[13] Y. M.Shin, M. M. Hohman, M. P. Brenner, and G. C. Rutledge, Appl. Phys. Lett. **78**, 1149 (2001).
[14] J. J. Feng, Phys. Fluids **14**, 3912 (2002).
[15] S. A. Theron, E. Zussman, and A. L. Yarin, Polymer **45**, 2017 (2004).
[16] A. L. Yarin, *Free Liquid Jets and Films: Hydrodynamics and Rheology* (Longman, Harlow/Wiley, New York, 1993).
[17] E. J. Hinch, *Perturbation Methods* (Cambridge University Press, Cambridge, 1991), pp. 42–45.
[18] J. R. Melcher and E. P. Warren, J. Fluid Mech. **47**, 127 (1971).
[19] S. Radev, B. Chavdarov, and I. Penchev, Theor Appl. Mech. **14**, 70 (1983).
[20] S. Radev, T. Asanuma, T. Iijima, and H. Ennoji, Proceedings of the Faculty of Engineering, Tokai University, Japan, 1984, Vol. 10, p. 69.
[21] S. Radev, Theor Appl. Mech. **16**, 57 (1985).
[22] B. Tchavdarov, S. Radev, P. Gospodinov, T. Iijima, and T. Asanuma, Proceedings of the Faculty of Engineering, Tokai University, Japan, 1988, Vol. 14, p. 23.
[23] S. Chandrasekhar, *Hydrodynamic and Hydromagnetic Stability* (Claredon, Oxford, 1961), Chap. XII.
[24] Lord Rayleigh, Philos. Mag. **34**, 145 (1892).
[25] C. Weber, Z. Angew. Math. Mech. **11**, 136 (1931).
[26] W. K. H. Panofsky and M. Phillips, *Classical Electricity and Magnetism* (Addison-Wesley, Reading, MA, 1962).
[27] A. L. Yarin, S. Koombhongse, and D. H. Reneker, J. Appl. Phys. **90**, 4836 (2001).
[28] G. I. Taylor and A. D. McEwan, J. Fluid Mech. **22**, 1 (1965).
[29] L. D. Landau and E. M. Lifshitz, *Fluid Mechanics*, 2nd ed. (Pergamon, Oxford, 1987).
[30] D. A. Saville, Phys. Fluids **14**, 1095 (1971).
[31] A. L. Yarin, J. Eng. Phys. **37**, 904 (1979).
[32] H. Xu, Ph.D. thesis, The University of Akron, 2003.
[33] N. Lynnerup, M. Andersen, and H. P. Lauritsen, Isozymes Curr. Top Biol. Med. Res. **5**, 156 (2003); RHINO3D (Robert McNeel & Associates, Seattle, WA, 2001), http://www.rhino3d.com; PHOTOMODELER (Eos Systems Inc., Vancouver, Canada, 2005), http://www.photomodeler.com